Journal of Catalysis 276 (2010) 360–370

Contents lists available at ScienceDirect

Journal of Catalysis

journal homepage: www.elsevier.com/locate/jcat

Gold supported on metal-doped ceria catalysts (M = Zr, Zn and Fe) for the preferential oxidation of CO (PROX)

O.H. Laguna *, F. Romero Sarria, M.A. Centeno, J.A. Odriozola

Departamento de Química Inorgánica e Instituto de Ciencia de Materiales de Sevilla, Centro Mixto Universidad de Sevilla-CSIC, Avenida Américo Vespucio 49, 41092 Seville, Spain

ARTICLE INFO

Article history:
Received 3 August 2010
Revised 28 September 2010
Accepted 28 September 2010
Available online 1 November 2010

Keywords:
Doped ceria
Oxygen vacancies
Gold catalysts
CO oxidation
PROX

ABSTRACT

A series of ceria oxides doped with 10 mol.% of Zr, Zn and Fe have been prepared by a pseudo sol–gel method throughout the thermal decomposition of the corresponding metallic propionates. With these supports, 1 wt.% gold catalysts were prepared by the deposition–precipitation method. All the solids were characterized by means of XRF, N_2 adsorption, XRD, Raman spectroscopy and SEM techniques, and their catalytic activity toward preferential oxidation of CO (PROX) reaction tested. The results showed solid solution when doping with Zr and Fe and ZnO surface segregation in the case of Zn. We demonstrate that gold dispersion depends on not only the oxygen vacancy concentration but also the nature of the doping agent. Finally, the catalytic activity was highly promoted by gold in all cases, being the doped gold catalysts more active than Au/CeO_2 at low temperature.

1. Introduction

Currently, important efforts have been focused on searching renewable energy sources looking for alternatives that can replace the fossil fuel [1]. Among all the proposed alternatives, in the long-term, hydrogen seems to be the most suitable fuel since its clean combustion preventing the emission of carbon-based pollutants or greenhouse gases [2]. Hydrogen production through the reforming of hydrocarbons either from fossil or from renewable sources seems to be the best option in the short-term; however, the reformate is a mixture of H_2 and carbon oxides as the main products [3]. For fueling PEM fuel cells hydrogen must contain ultralow levels of carbon monoxide (typically bellow 10 ppm) to prevent poisoning of the Pt-based PEMFC catalyst [4]. Therefore, to reduce the CO levels in the reformate CO abatement processes must be applied. These are commonly composed of a combination of high- and low-temperature water gas shift reactions that allow decreasing the CO level in the reformate to 1–2% [5–7], and the preferential oxidation with air of the pre-cleaned reformate (PROX) is a cheap and effective solution, since the range of working temperature matches the one at which PEM fuel cells operate [8].

PROX reaction requires selective catalysts able to remove CO without oxidize H_2, an undesired side reaction. CeO_2-based catalysts have been widely used [9] mainly due to its redox properties (Ce^{4+}/Ce^{3+}) that allow an easy oxygen exchange with the medium. Several studies have demonstrated that doping of CeO_2 with elements of different ionic radii or oxidation state improves the exchange of oxygen in the oxide network by decreasing the energy barrier for oxygen migration [10–12]. The synergy between the ceria and the modifier can be achieved throughout different mechanisms, such as the formation of a solid solution [10,13], the interaction between segregated oxides [14–16] and the deposition of metallic particles over the surface [17,18].

Given the effects generated by ions with lower reduction state and smaller sizes than Ce^{4+}, there is a considerable scientific interest in doping ceria with different elements. For example, Ce and Zr oxides form solid solution in the whole range of compositions [19–22]. In the case of Ce–Fe systems, although the solubility of iron into the CeO_2 network is low, the formation of a solid solution has been demonstrated [10], but some works also report the segregation of iron oxides when the amount of iron is above a certain value [11,23]. On the other hand, Zn has also been used as a CeO_2-doping agent; however, the formation of solid solution has not been reported, being the segregation of well-dispersed ZnO over the CeO_2, the main mechanism of interaction in this case [24].

Ceria-modified mixed oxides are promising supports for noble metals catalysts because the interaction of the metallic particles with the ceria at the surface is increased, promoting the metallic dispersion [5,20]. From the notable discovery by Haruta [25] that highly dispersed Au nanoparticles are extremely active in CO oxidation reactions, the interest in the application of gold catalysis has grown dramatically. However, a number of issues remain unresolved concerning the structure and the mechanism of this kind of catalyst, while the relevance of the size and morphology of the Au

* Corresponding author. Fax: +34 954460665.
E-mail address: oscarh@icmse.csic.es (O.H. Laguna).

0021-9517/$ - see front matter © 2010 Elsevier Inc. All rights reserved.
doi:10.1016/j.jcat.2010.09.027

particles, the oxidation state of gold and the chemical nature of the supports as well as the presence and type of the support defects are well established for the catalytic performances of gold catalysts [26,27].

In previous works, we have shown that the support structural defects play a key role on the activity of gold catalysts in the oxidation of CO, increasing the catalytic activity with the number of defects; similarly, defect generation during the CO oxidation reaction influences gold dispersion contributing to gold surface dynamics [28–30]. Therefore, the modification of the ceria network with different cations will result in modified defect structures that will depend on the nature of the modifier. The study of the effect of the interaction of these modified supports with metallic gold particles and their influence in the catalytic activity in the PROX reaction will allow understanding the synergy in these systems, considering the specific characteristics of every catalyst.

The evaluation of the structural effects caused by the doping element on the CeO_2 network, as a function of the chemical nature of the modifier (Zr, Zn and Fe) and how these defect structures influence gold deposition will allow a correlation between the main physicochemical properties of the catalysts and their catalytic activity on the PROX reaction. For that, X-ray fluorescence (XRF), N_2 adsorption, X-ray diffraction (XRD), Raman spectroscopy, scanning electronic microscopy (SEM) and temperature-programmed reduction (TPR) techniques have been used.

2. Materials and methods

2.1. Synthesis

A series of Ce–M (M = Zr, Zn, Fe) mixed oxides, with a Ce/M molar ratio of 9/1, were synthesized by modifying a reported pseudo sol–gel method involving the thermal decomposition of the propionates [31–33]. These mixed propionates were produced after dissolution of the adequate amounts of Ce(III) acetate (Aldrich), Zr(IV) acetyl acetonate (Aldrich), Zn(II) acetyl acetonate (Fluka) and Fe(III) acetyl acetonate (Fluka) in propionic (Alfa Aesar) acid (0,12 M). For every mixture, the propionic acid excess was distilled until obtaining a kind of resin that was calcined at 500 °C (2 °C/min) for 2 h. Pure CeO_2 was synthesized by the same procedure for comparative purposes. The nomenclature of the oxides indicates the amount of doping metal expressed as molar percentage mol.% (CeO_2, CeZr10, CeZn10 and CeFe10).

The gold-containing catalysts were prepared by deposition–precipitation. The adequate amount of $HAuCl_4{\cdot}3H_2O$ to obtain 1% w/w of gold in the support was dissolved in deionized water (6.0×10^{-4} M), and the pH of the solution was adjusted to 8 by addition of NaOH 0.1 M with an automatic system of measurement and titration (CRISON pH-Burette 24). This pH value has been reported as adequate for a successful deposition of gold on ceria surfaces [33–35]. The solution was heated to 70 °C, and then the support was added and kept under continuous stirring for 20 min. The obtained solid after filtration was washed with distilled water several times (until the disappearance of Cl^- and Na^+ ions), then dried overnight at 100 °C and finally calcined for 2 h at 300 °C [29].

2.2. Characterization

The elemental composition of the samples was determined by X-ray fluorescence (XRF) spectrometry in a Panalytical AXIOS PW4400 sequential spectrophotometer with Rh tube as source of radiation. The measurements were taken onto pressed pellets containing 6 wt.% of wax.

The textural properties were studied by N_2 adsorption/desorption measurements at liquid nitrogen temperature in a Micromeritics ASAP 2010 apparatus. Before analysis, the samples were degassed at 150 °C for 2 h in vacuum.

Powder X-ray diffraction (XRD) patterns were recorded on a Siemens D500 diffractometer, using Cu Kα radiation (40 mA, 40 kV), with 0.05° step size and 1 s of step time, over a 2θ range from 10° to 80°.

Raman spectra were recorded on a dispersive Horiva Jobin Yvon LabRam HR800 microscope with a 20-mW green laser (532.14 nm) without filter and using a 600 grooves/mm grating. The microscope used a 50× objective with a confocal pinhole of 10 μm.

Scanning electron microscopy (SEM) analyses of the supports were carried out in a SEM-FEG Hitachi S4800 instrument equipped with an energy dispersive X-ray analyzer (EDX). A Zeiss ULTRA 55 high-resolution FESEM equipped with in lens, secondary and backscattered detectors were used for analyzing the gold particle size distribution.

Temperature-programmed reduction (TPR) experiments were carried out in a conventional quartz reactor connected to a TCD. The reactive gas stream (5% H_2 in Ar) was flowed at 50 mL/min over 50 mg of sample, and the temperature raised at 10 °C/min from room temperature to 900 °C. A molecular sieve 13X was used to retain the H_2O produced during the reduction and CO_2 that could be desorbed on the surface of the solid. Quantitative analysis was done by integration of the reduction signal and comparison with hydrogen consumption of a CuO reference.

2.3. Catalytic activity (preferential oxidation of CO PROX)

PROX reaction was carried out at atmospheric pressure on a cylindrical stainless steel reactor (9 mm inner diameter), with 100 mL/min of a reaction mixture containing 2% CO, 1% O_2, 50% H_2 and N_2 as balance. In order to avoid intrareactor gradients, the catalyst powder (100 mg, particle size ∅ = 100–200 μm) was diluted with crushed inert glass with the same particle size until a reactor bed height of 5 mm. Before reaction, samples were activated for 1 h at 300 °C with a 21 vol.% O_2 in N_2 flow (30 mL/min). Products and reactants were separated by online gas chromatography (Agilent® 7890, equipped with a Porapak® Q, two Molecular Sieve 5A, and two Hayesep® Q columns) and then quantified using a TCD detector.

The CO conversion was calculated according to Eq. (1) where CO_{in} is the amount of the CO in the inlet and CO_{out} is that of the outlet.

$$CO_{conversion}\ (\%) = \frac{(CO_{in} - CO_{out}) \times 100}{CO_{in}} \quad (1)$$

The O_2 selectivity to CO_2 formation was calculated with the Eq. (2). O_{2in} corresponds to oxygen in the inlet and O_{2out} to that in the outlet.

$$O_{2Selectivity}\ (\%) = \frac{(CO_{in} - CO_{out}) \times 100}{2(O_{2in} - O_{2out})} \quad (2)$$

Rearranging Eq. (2), it is possible to derive an expression that correlates the CO conversion with the O_2 selectivity to CO_2.

$$O_{2Selectivity}\ (\%) = CO_{conv} \times \frac{CO_{in}}{2(O_{2in} - O_{2out})} \quad (3)$$

From the thermodynamic point of view, 100% oxygen conversion must be attained, and therefore O_2 selectivity to CO_2 and CO conversion are linearly correlated with a slope equal to half the CO-to-O_2 stoichiometric ration, if the thermodynamic limit is reached, Eq. (4).

$$O_{2Selectivity}\ (\%) = CO_{conv} \times \frac{CO_{in}}{2 \cdot O_{2in}} \quad (4)$$

3. Results

3.1. Chemical and textural analysis

The chemical composition of the prepared solids is presented in Table 1. All solids have metallic contents very close to the target ones (10 mol.%). In the same way, gold catalysts have a gold content around the intended value (1 wt.%).

Concerning the textural properties, all samples are mesoporous materials with pore sizes around 110 Å. The solid CeZr10 has the highest BET surface area and pore volume, ≈30% higher than those of the bare CeO_2 and CeZn10 and CeFe10 solids. Deposition of gold does not promote any important change in the textural characteristics of the support. Only a slight increase in the average pore size and pore volume is detected in all the gold samples.

3.2. XRD

The XRD patterns of the prepared supports are presented in Fig. 1. For all samples, the diffractograms correspond to the *c*-CeO_2 fluorite structure (JCPDS 00-034-0394). However, a shift to higher diffraction angles of the main reflections is observed in some samples compared with that of pure CeO_2, suggesting the modification of the cell parameter by the substitution of cerium cations by the doping agent in the CeO_2 network. For all the considered solids, the calculated cell parameters are presented in Table 2.

Those supports containing Zr and Fe present a lower cell parameter than that of pure ceria. However, CeZn10 solid has the same cell parameter. On the other hand, in Table 2, the average crystallite size of the solids, calculated using the Scherrer equation, is also shown. All modified supports present a lower crystallite size than those of the synthesized pure ceria, being CeZr10 the solid with the lowest value.

In the case of the support modified with Zn, a close analysis of the XRD pattern (Fig. 2) shows two weak signals that can be assigned to the presence of zincite (ZnO) (JCPDS 36-1451) [36]. Those reflections could be indexed to the (1 0 0) and (0 0 2) crystallographic planes.

Gold catalysts present a similar XRD pattern than the corresponding support, without any observable shift in the position or in the width of their diffraction lines. Moreover, no signals due to the presence of metallic Au could be detected (Fig. 1).

3.3. SEM

Selected SEM micrographs of the prepared supports are shown in Fig. 3. Pure CeO_2 has a laminated morphology, the layers being composed by wormlike aggregates allowing the formation of a kind of mesoporosity (10–15 nm, Fig. 3a).

The Zr-modified support has lost the layered morphology, and only aggregates randomly placed are observed (Fig. 3b). In the case of the CeFe10 and especially, for the CeZn10 solid, among these aggregates, some sheets similar to those of the pure ceria remain

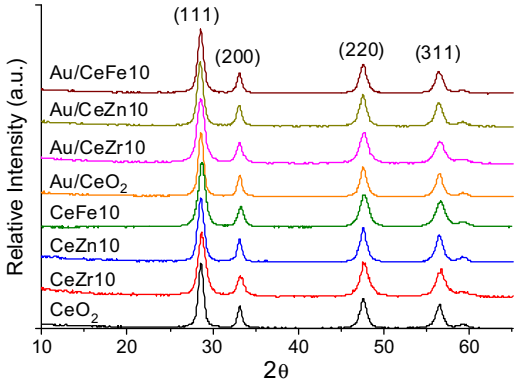

Fig. 1. XRD patterns of the prepared solids.

Table 2
Cell parameter and crystal size of the prepared solids.

Solid	Cell parameter, *a* (Å)[a]	Crystallite size (Å)[b]
CeO_2	5.405	142
CeZr10	5.339	81
CeZn10	5.406	124
CeFe10	5.383	119
Au/CeO_2	5.403	148
Au/CeZr10	5.338	91
Au/CeZn10	5.400	120
Au/CeFe10	5.380	117

[a] Calculated from the *a* average of the planes (1 1 1), (2 0 0), (2 2 0), (1 1 3).
[b] Calculated with the Scherrer equation.

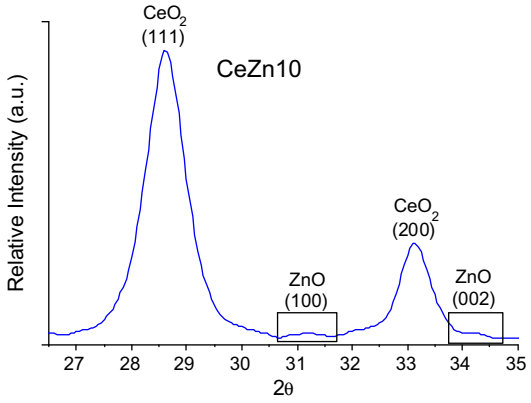

Fig. 2. XRD pattern of the CeZn10 support.

Table 1
Chemical composition and main textural properties of the prepared solids.

Solid	Ce (mol.%)[a]	M[b] (mol.%)	Au (wt.%)	S_{BET} (m^2/g)	Average pore size (Å)	Pore volume (cm^3/g)
CeO_2	100	–	–	53	110.5	0.1773
CeZr10	89.7	10.3	–	70	115.3	0.2448
CeZn10	89.6	10.4	–	56	112.9	0.1802
CeFe10	89.2	10.8	–	55	116.2	0.1709
Au/CeO_2	100	–	1.0	54	115.0	0.2001
Au/CeZr10	89.7	10.3	1.0	65	135.0	0.2444
Au/CeZn10	89.6	10.4	1.1	62	120.0	0.2571
Au/CeFe10	89.2	10.8	0.9	59	126.5	0.2310

[a] Ce mol.% = 100 × $mol_{Ce}/[mol_{Ce} + mol_M]$/M mol.% = 100 × $mol_M/[mol_{Ce} + mol_M]$.
[b] M = Zr, Zn or Fe.

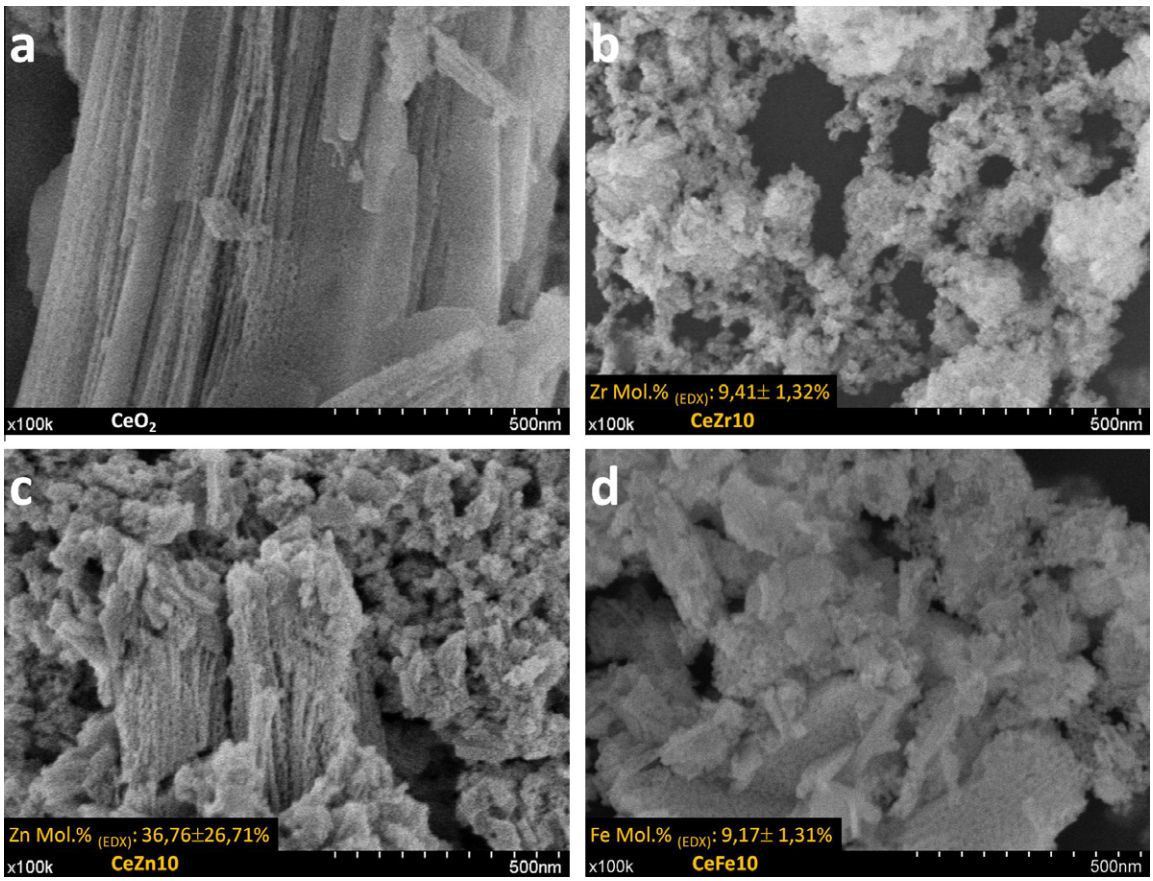

Fig. 3. SEM micrographs of the prepared supports: (a) CeO_2; (b) CeZr10; (c) CeZn10; (d) CeFe10.

distinguishable (Fig. 3c and d). The chemical composition at the surface of the mixed oxides which was established by means of EDX analyses is presented in the respective micrograph for every support. The average mol.% of every doping agent on the surface shows that supports modified with Zr and Fe present a doping content very close to the intended one with a low deviation. On the other hand, the solid with Zn presented a heterogeneous composition, depending on the position of the EDX analysis and the Zn mol.% is above the expected one (10%), with a high deviation.

For the corresponding gold catalysts, SEM micrographs are presented in Fig. 4; the morphology of the supports remains almost unaltered without noticeable major changes. The presence of gold nanoparticles (viewed as small grains with the highest brightness) with diameters between 4 and 19 nm can be established for all the materials in the micrographs (Fig. 4). However, the density of those detected gold nanoparticles is higher for the Au/CeO_2 (Fig. 4a) than for the other doped catalysts. Gold nanoparticles with diameters below 4 nm cannot be detected since for magnifications as high as 100,000× one image pixel corresponds to diameters above 1 nm. SEM images clearly establish that gold dispersion is higher in the modified ceria supports since only isolated detectable gold particles are observer, while for the unmodified support a whole range of gold particle diameters are observed in Fig. 4.

3.4. Raman spectroscopy

The Raman spectra of the supports are presented in Fig. 5. For pure CeO_2, two main bands can be seen. The strong one at 460 cm^{-1} is assigned to the F_{2g} Raman active mode of CeO_2 fluorite structure, which can be viewed as a symmetric breathing mode of the oxygen atoms around Ce^{4+} ions [37,38]. The second band at ca. 600 cm^{-1} has been widely reported in literature and is associated with the presence of the oxygen vacancies preferentially placed on the surface of the cubic structure of the CeO_2 [11,37,38].

The position and width of these two bands change in the modified supports, slightly in the case of CeZr10 and CeZn10 solids, but in a strong way in the case of the Fe-modified sample. In this support, the F_{2g} band broads and shifts toward 440 cm^{-1}, while the oxygen vacancies band seems to disappear or is overlapped with the F_{2g} one. Several factors could be responsible of such behavior: changes in the structure, particle size, sizes distribution, number and nature of defects, nature and concentration of doping cations, among others [11,37,38]. As all these factors influence in a similar way both bands, it is well accepted that the correct way of evaluating the amount of oxygen vacancies of a sample is to measure the ratio between the areas of the oxygen vacancies band (Ov) and the F_{2g} band, in such a way that the higher the Ov/F_{2g} ratio, the higher the number of oxygen vacancies [11,38]. The results obtained for the considered supports are presented in Fig. 6. CeZn10 solid has a similar amount of oxygen vacancies that pure CeO_2. However, the number of oxygen vacancies strongly increases in the CeZr10 solid and is decreased when ceria is modified with iron.

The Raman spectra of the gold catalysts are shown in Fig. 7. The oxygen vacancies band is absent in all spectra. In addition, the CeO_2 F_{2g} band is always broader than that of the corresponding support (Fig. 5). Besides this, the band shifts to lower frequencies, especially in the case of the catalysts with Zr and Fe.

3.5. TPR

The TPR profiles of the prepared supports are shown in Fig. 8. Pure CeO_2 exhibits two broad reduction peaks. The first one cen-

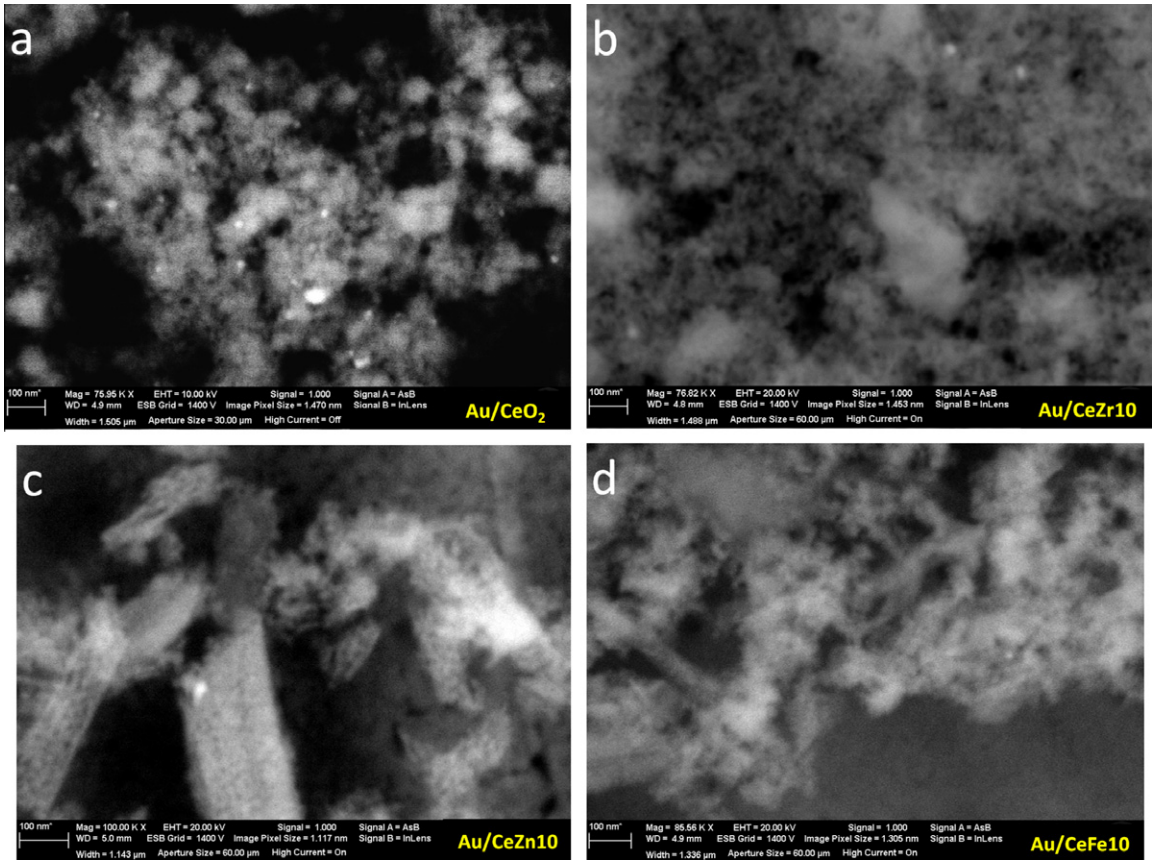

Fig. 4. SEM micrographs of the prepared gold catalysts: (a) Au/CeO_2; (b) Au/CeZr10; (c) Au/CeZn10; (d) Au/CeFe10.

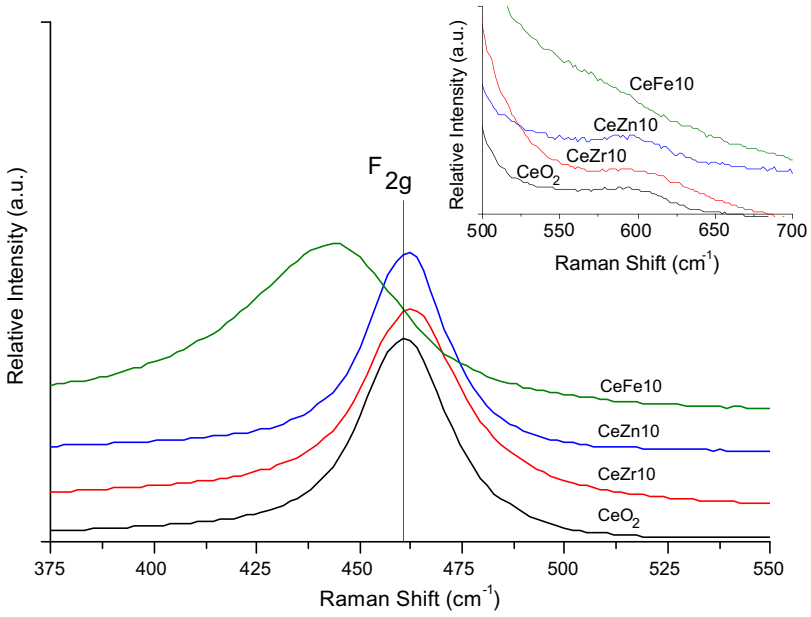

Fig. 5. Raman spectra of the prepared supports.

tered around 495 °C and the second one, more intense, at around 781 °C.

The TPR profile of the CeZr10 support is relatively similar to that of pure CeO_2. Two reduction peaks around the same temperatures (495 and 781 °C) appear, but the area ratio between them changes, the lower-temperature peak becoming the biggest one. In the case of the CeZn10 solid, the TPR profile is also similar to that of pure CeO_2, but a third reduction peak at lower temperature (386 °C) is present.

For the CeFe10 system, the high-temperature H_2 consumption appears at 760 °C, 20 °C below the high-temperature reduction peak of pure CeO_2. Additionally, this signal presents a broad shoul-

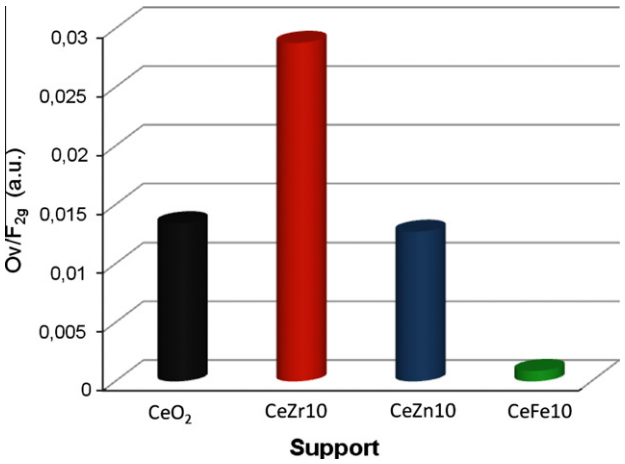

Fig. 6. Ov/F_{2g} ratio for the doped supports.

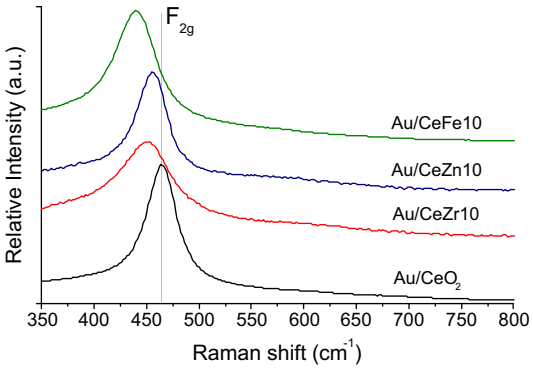

Fig. 7. Raman spectra of the studied gold catalysts.

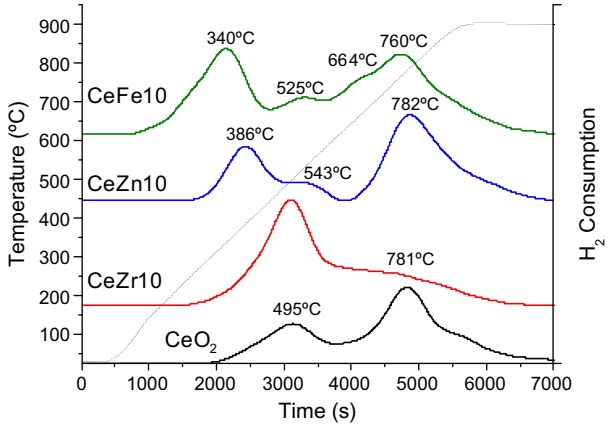

Fig. 8. TPR profile of the prepared supports.

der at 664 °C. Besides this, a small signal can also be detected around 525 °C. Finally, an intense and broad H_2 consumption is observed at lower temperatures (340 °C).

The TPR profiles of gold catalysts are presented in Fig. 9. The Au/CeO_2 solid has a high-temperature peak at around 780 °C. At lower temperatures, a new small peak appears (443 °C). The especial feature of this TPR profile is the presence of an intense signal at very low temperatures, around 189 °C, which is not present in the CeO_2 TPR profile (Fig. 8).

In the case of the Au/CeZr10, there is a high-temperature reduction peak with maximum at 746 °C. This signal has a very broad

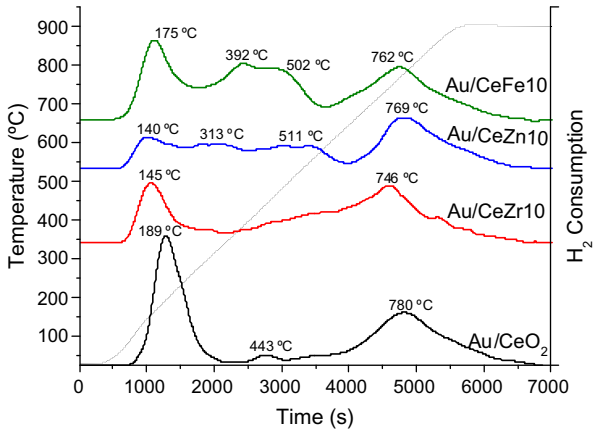

Fig. 9. TPR profile of the studied gold catalysts.

shoulder at lower temperature, which extends until 300 °C. Finally, a low-temperature reduction process, around 145 °C, which is not observed for the CeZr10 support, appears.

For the gold catalyst doped with Zn, there is also a broad high-temperature peak around 769 °C. From 248 °C to 647 °C, there is an overlapped group of signals. At lower temperatures, an additional peak can be differentiated with maximum at 140 °C.

In the case of the Au/CeFe10 solid, the high-temperature peak appears around 762 °C. At intermediate temperatures, there is a combination of at least two additional reduction events (392 °C and 502 °C). Finally, at lower temperatures, a reduction process can be established around 140 °C.

3.6. Catalytic activity

The CO conversion of the supports in the PROX reaction is presented in Fig. 10. Although the catalytic activity of all solids is low, modified supports have always a higher one than pure CeO_2, as already reported for the CO oxidation in WGS [39] or PROX [9,16,28] reactions.

The catalytic activity shown by the gold catalysts is presented in Fig. 11. As expected, gold catalysts are more active than the corresponding supports. In the case of Au/CeO_2 system, the catalytic activity is considerably improved from 120 °C, temperature at which the solid begins to be reduced in hydrogen (Fig. 9), pointing out that the catalytic activity is intimately connected with the promotion of the reducibility.

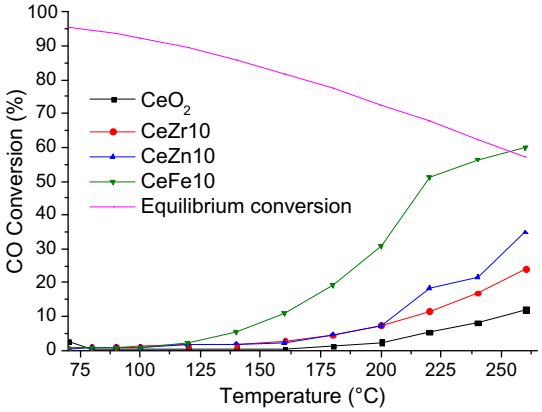

Fig. 10. CO conversion during the PROX reaction over the studied supports.

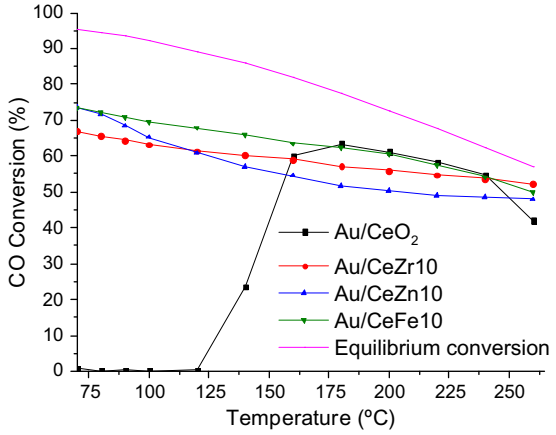

Fig. 11. CO conversion during the PROX reaction over the studied gold catalysts.

The promoting effect is more evident for the doped catalysts. For these catalysts, the CO conversion starts at temperatures below 75 °C. The trend for the three doped catalysts is quite similar; however, the Au/CeFe10 catalyst shows a slightly better catalytic activity than the other gold catalysts. In all cases, a 100% CO conversion is not achieved, which is associated with the existence of side reactions: H_2 oxidation and the reverse water gas shift reaction (R-WGS) [40] (presented in Eqs. (5)and (6)).

$$H_2 \text{ oxidation} : H_2 + \frac{1}{2}O_2 \rightarrow H_2O \quad (5)$$

$$\text{R-WGS} : CO_2 + H_2 \Longleftrightarrow CO + H_2O \quad (6)$$

On the other hand, the similar behavior of the gold-doped catalysts (Au/CeZr10, Au/CeZn10 and Au/CeFe10) seems to indicate that the catalytic activity is not determined by the type of interaction between the doping metal (Zr, Zn or Fe) and the Ce, but for gold dispersion.

4. Discussion

4.1. Supports

The chemical composition of the supports (Table 1) matches well the intended one, evidencing that the thermal decomposition of the propionates method allows obtaining materials with a controlled stoichiometry, as already reported [31,32]. However, the generated structures and their textural and morphological properties depend on the metal doping nature. CeZr10 support has BET surface area and pore volume values above those of the other systems (Table 1). This correlates with the modification of the layered morphology of the ceria after zirconium doping observed by SEM (Fig. 3). In the same way, this solid shows the lowest cell parameter and crystal size of the prepared supports (Table 2). The decrease in the cell parameter of ceria after zirconium doping has been widely reported and suggests the formation of a solid solution [39,41], since the introduction of Zr^{4+} in the CeO_2 fluorite structure results in a contraction of the unit cell due to the smaller ionic radii of Zr^{4+} compared with that of Ce^{4+} [20,42].

In an opposite way, Zn does not generate important modifications in the textural properties of the bare ceria. Additionally, no contraction of the fluorite cubic structure of CeO_2 is evidenced throughout the XRD measurements (Table 2). This correlates with the detection by XRD of characteristic reflections of ZnO (Fig. 2) and the heterogeneous and higher surface concentration of Zn compared with the bulk one, evidenced by EDX. These results agree with the surface segregation of Zn and the non-effective introduction of this cation into the ceria network. Similar conclusions were reported by Papavasiliou et al. [24] for $CuCe_{0.95}Zn_{0.05}$ and $CuCe_{0.80}Zn_{0.2}$ mixed oxides from XPS analyses.

In the case of the solid doped with Fe, the observed decrease in the cell parameter with respect to that of pure ceria (Table 2) and the absence of XRD lines due to iron oxide species evidence the formation of a solid solution [10,11,43]. No changes in the surface area BET or pore volume values are detected, although the enhancement in the average pore size and the SEM observations suggest the evolution of a new porosity by the introduction of Fe inside the CeO_2 structure.

The different interaction between the doping metals and CeO_2 is also confirmed from Raman spectroscopy. The observed shift and broadening of the F_{2g} peaks are due to the alteration in the relaxation energy of the cubic structure [37]. This behavior has been associated with structural modifications by the doping effect [37,44]. In our case, the observed decrease in the ceria particle size in the doped samples calculated by the Scherrer equation (Table 2) could agree with the shift and/or broadening of the F_{2g} peak (Fig. 5). In all supports, the presence of doping metals inhibits the sintering of the CeO_2 particles during the calcination. This behavior has been previously reported [45], especially for solid solution structures. In good agreement, our supports with the lower particle size are those where the formation of a solid solution has been demonstrated (CeZr10 and CeFe10). In these systems, the surroundings of the Ce cations are modified by the doping metals, and the vibration symmetry of the oxygen atoms around the metallic ions is different [37] depending the particular vibration energy on the chemical nature of the metallic modifier. This has been early discussed by Xiao et al. [13] for CeO_2 doped with Y, La, Pr, Zr and Sn. They reported different Raman shifts of the ceria F_{2g} band as a function of the doping cation nature. The strong interaction of iron with ceria could be the reason of the strong shift and higher width of the F_{2g} band in the CeFe10 solid compared with those in CeZr10 one, in spite of the lower particle size of the later. According to all above, the observed changes in the ceria Raman F_{2g} band are due, among other factors, to changes in the ceria crystal size and in the symmetry of the cubic structure of ceria which depends on the doping nature.

On the other hand, the presence of the oxygen vacancies Raman band on CeO_2 supports (Fig. 5) indicates the existence of reduced Ce^{3+} species. As previously discussed for Eu [37]- and Pr [46]-doped ceria, the detection and relative intensity of this Raman band are affected by many factors. In particular, those factors affecting the absorption and Raman scattering effect, such as the laser power and frequency, the particle size distribution and homogeneity of the material and the absorption properties of the solid, are relevant since they determine the penetration depth of the Raman radiation.

In a paper about Ce–Eu mixed oxides that were analyzed under the same conditions used in this work [37], it was demonstrated that most of the information was extracted from the surface of the material. From here and because of the similar absorption properties of the solids (not shown), we can infer the main surface character of the oxygen vacancies detected in our supports. This is not surprise since defects such oxygen vacancies are preferably located on the surface in order to minimize the Gibbs free energy [12].

Concerning the amount of oxygen vacancies evaluated from the Ov/F_{2g} Raman ratio (Fig. 6), Zn-doped support has a similar amount than that observed for pure ceria, which is in good agreement with the low Zn–Ce interaction and the observation of ZnO segregation. The solid with Zr presents a higher Ov/F_{2g} ratio which is expected because the introduction of Zr^{4+} ions increases the reducibility of Ce [47,48]. Finally, the solid with Fe shows the lowest amount of

oxygen vacancies of all prepared supports, confirming the solid solution formation [10,43].

A similar behavior has been reported by Bao and coworkers for Ce–Fe mixed oxides prepared by coprecipitation [11]. However, they established that the oxygen vacancies band disappears when the Fe molar ratio in the Ce–Fe solid reaches 0.4 and above. These authors reported that small doping amounts of Fe^{3+} facilitate the formation of oxygen vacancies, whereas large doping amounts annihilate them. This could be attributed to two different doping mechanisms to balance the charge when Ce^{4+} is substituted by trivalent Fe^{3+} cation. One is the vacancy compensation mechanism [49], which promotes the generation of oxygen vacancies and the other is the dopant interstitial compensation mechanism, which eliminates them [11], In our case, due to the observed reduction in the number of oxygen vacancies, we can deduce that the interstitial compensation mechanism is prevailing, even for the low amount of iron introduced (10 mol.%). From here, it must be pointed out that the thermal decomposition of the propionates method promotes the interaction of Fe with the oxygen vacancies of the ceria network, compared with the coprecipitation method followed by Bao et al. [11].

Additional information of the Ce–doping metal interaction can be extracted from the TPR analyses. The two reduction peaks observed for pure CeO_2 (Fig. 8) have been widely reported and assigned to the reduction of the surface shell (low-temperature peak) and bulk reduction (high-temperature one) [50]. CeZr10 support has the same reduction steps but, in this case, the shell reduction becomes more intense than the bulk reduction. Therefore, an enhancement of the surface CeO_2 reducibility due to the incorporation of Zr is evident. This agrees with the reported promoting effect of the Zr in the oxygen mobility in CeO_2, and the stabilization of Ce^{3+} species is due to the formation of a solid solution [48,50].

In the case of the CeZn10 solid, it is difficult to correlate the reduction peaks with the reduction processes since Zn^{2+} reduction can also be produced. In this sense, Avgouropoulos et al. [16] established that Zn promotes the reducibility of Au/CeO_2 catalysts at lower temperatures by increasing the oxygen mobility. A similar promoting effect of Zn on the reducibility of many other catalytic systems has been widely reported, for instance CuO–ZnO/TiO, [36] Pt/ZnO [51,52] and Pt/CeZn [20].

Although pure ZnO does not have a high intrinsic reducibility, Zn^{2+} reduction can be achieved when it is in close contact with other metallic ion by synergy between the mixed cations, as was demonstrated by Naknam et al. [53].

Therefore, the lowest-temperature signal of the CeZn10 support (386 °C) could be attributed to the reduction of Ce^{4+} and Zn^{2+} in close contact. The second reduction step (543 °C) is probably due to the reduction of the surface Ce^{4+} species not interacting with Zn. The presence of two surface Ce^{4+} reduction peaks agrees with the heterogeneity of the surface Zn distribution, probably as ZnO, demonstrated by XRD and SEM and EDX analyses (Fig. 3). Finally, the peak at 782 °C must be associated with bulk CeO_2 reduction.

For the CeFe10 support, not only Ce^{4+} reduction but also Fe species ones must be considered [54]. The broad zone observed around 760 °C (Fig. 8) corresponds principally to the reduction of the bulk ceria. This temperature is 20 °C below those of the bulk reduction of the other supports, showing the synergic effect between Ce and Fe that improves the reduction of the mixed oxide. The broadening of this signal can also be due to the reduction of FeO to metallic Fe. The differentiation and identification of specific reduction steps in the 400–600 °C region is especially difficult, because the reduction of surface Ce^{4+} occurs simultaneously with that of Fe_3O_4 to FeO [54]. Finally, the reduction of surface Ce^{4+} species and Fe_2O_3 to Fe_3O_4 must be overlapped in the intense reduction peak observed at lower temperature (340 °C).

4.2. Gold catalysts

In all catalysts, the deposited amount of gold corresponds to the target value. After the gold deposition, the textural properties of the supports are hardly modified; just a slight increment in the average pore size could be related to the presence of gold nanoparticles inside the porous structure of the supports as previously reported [55,56]. The average particle size of the gold nanoparticles is small enough for preventing the observation of gold diffraction lines in the XRD patterns of the catalysts (Fig. 1). Nevertheless, the presence of gold is confirmed by XRF and high-resolution SEM micrographs, Fig. 4.

Indeed, the observed gold particles have diameters between 4 and 19 nm; however, the Au/CeO_2 catalysts presents a higher density of these nanoparticles in comparison with the other gold catalysts, Fig. 4a–d. Considering that all the catalysts have similar amounts of deposited gold, this indicates that particles having diameters below 4 nm cannot be detected in the high-resolution FESEM analyses being the proportion of these smaller gold clusters higher for the Zr-, Zn- and Fe-doped gold catalyst than for Au/CeO_2. This demonstrates a higher noble metal metallic dispersion over the doped solids [34,57], pointing to the generation of preferential surface sites for gold deposition over the ceria surface upon modification with Zr, Zn and Fe.

These preferential surface sites can be correlated with the higher amount of oxygen vacancies for the CeZr10 support than for the pure CeO_2 support. The nucleating sites for gold in the Au/CeZn10 support may be associated with the surface sites where the Ce–Zn interaction is stronger, probably at the periphery of the supported ZnO islands. The formation of solid solution when doping with iron and the decrease in the amount of oxygen vacancies in the CeO_2 structure indicate that iron is occupying interstitial positions in the ceria lattice; therefore, upon doping not only octahedral sites of the ceria lattice are occupied but also tetrahedral ones, these generate new surface sites where the deposition of gold is also promoted, Fig. 4d.

The shift and broadening of the CeO_2 F_{2g} Raman band in the gold catalysts compared with those of the corresponding supports is an evidence of the gold–support interaction, gold modifying the surroundings of the support surface species because of an epitaxial contact between Au and the oxide. The surface Ce cations suffer a distortion of their cubic symmetry by the interaction with the electronic density of gold. Other remarkable aspect upon gold deposition is the disappearance of the band assigned to oxygen vacancies whatever the support. Since, as stated above, the oxygen vacancies detected by Raman are mainly placed at the surface of the solid; oxygen vacancies act as preferential sites for the nucleation of gold nanoparticles, and therefore their disappearance must be associated with the gold anchoring process. This behavior of the oxygen vacancies has been discussed by Qian and coworkers in their studies over $Au/CeO_2/SiO_2$ catalysts for the CO oxidation [58]. According to this, the higher the amount of oxygen vacancies in the initial support, the higher the number of nucleation sites of the gold particles and lower the average size and higher the metallic dispersion of gold as demonstrated by SEM studies (see Figs. 4 and 6). In the case of CeFe10 support, where the oxygen vacancies band is difficult to detect or even is absent (Fig. 6), Fe dispersed in the CeO_2 structure generates in the support surface strategic sites for the deposition of gold. The presence of Fe (with a lower oxidation state than cerium) in interstitial sites creates structural sites where the coordination of the Fe cations is four and, consequently, with an increased electronic density which could act in a similar way that oxygen vacancies, being sites for the preferential deposition of the gold nanoparticles (Fig. 4d).

TPR profiles of gold catalysts are shown in Fig. 9. The high-temperature reduction peak occurs at similar temperatures for the

Table 3
H_2 consumption for the lowest-temperature peak (LTP) for the studied gold catalysts.

Solid	H_2 consumption* LTP μmol of $H_2/g_{catalyst}$	Theoretical H_2 consumption if Au^{3+} μmol of $H_2/g_{catalyst}$	Theoretical H_2 consumption if Au^{+} μmol of $H_2/g_{catalyst}$
Au/CeO_2	709.8	73.9	24.0
Au/CeZr10	379.2	75.5	24.5
Au/CeZn10	288.4	83.2	24.0
Au/CeFe10	578.6	73.9	24.0

* Hydrogen consumption for the lowest-temperature peak in Fig. 9.

supports and the gold catalysts. As for the supports, this peak is assigned to the ceria bulk reduction [50]. The deposition of gold does not affect the ceria bulk reduction mechanism as stated by the unmodified temperature of reduction of such bulk species. A broad feature corresponding to the reduction of surface Ce^{4+} species in different coordination environments occurs at lower temperatures (190–650 °C), (Fig. 9) [50]. For the solids containing other reducible metals than cerium, such as Fe or Zn, the hydrogen consumption due to the reduction of such metallic species is overlapped in this broad reduction range, as was described above for the respective supports [51–54,59]. The numerous overlapping reduction processes difficult the assignment of the different specific reduction peaks in this broad zone, especially for the systems doped with Zn and Fe. However, it is clear that the presence of the doping cations (Zr, Zn and Fe) increases the reducibility of Ce and that upon gold deposition, these signals become broader and occurs at lower temperatures. Beside this, a new reduction signal at temperatures below 190 °C, the lowest-temperature peak (LTP), appears in gold catalysts. This process has to be assigned to the reduction of surface Ce^{4+} in close contact with the gold nanoparticles. If the presence of cationic gold species was assumed, their reduction peak would overlap the described LTP process. The estimated amount of gold species considering Au^{3+} or Au^{+} cations is presented in Table 3. The hydrogen consumption achieved in the LTP peak is also presented for the sake of comparison. Although a contribution of the reduction of partially oxidized Au species cannot be fully discarded [26,27,60,61], the assignment of these LTP peaks to surface Ce^{4+} species reduction must be assumed from data in Table 3. It is clear that the close Au–Ce interaction enhances oxygen mobility and consequently the Ce^{4+} reducibility to Ce^{3+} [62]; however, the average oxidation state of gold cannot be clearly stated. In fact, the discussion about the reduction state of the deposited Au species in supported catalysts is a controversial point and is currently under debate, having been reported the presence of $Au^{\delta-}$ [63], Au^0 [26,60,61], Au^{+} and Au^{3+} species [27,45].

As stated above, the doping cations distort the cubic ceria structure (Zr and Fe) or the material surface (Zn). These distortions promote the creation of new anchoring sites for gold nanoparticles, increasing that way the metallic dispersion and resulting in smaller gold particles, which agrees with the absence of Au reflection in the XRD patterns (Fig. 1) and the small amount of gold nanoparticles detected by high-resolution FESEM analyses (Fig. 4). All these facts explain the observed higher reducibility of the doped supports compared with that of bare ceria, and of the gold catalysts compared with that of the corresponding support.

In order to have as quantitative estimation of the reducibility of the considered samples, the reduction percentage (RP) of every system has been calculated according to Eq. (7).

$$\mathrm{RP} = \frac{E_{HC}}{T_{HC}} \times 100 \qquad (7)$$

In this equation, T_{HC} is the theoretical hydrogen consumption (in moles) required for the complete reduction of all the reducible cations present in the solid and E_{HC} is the experimental total hydrogen consumption measured during the TPR. For the calculation of T_{HC}, we have considered that all cations are initially in their maximum oxidation state, except gold for which Au^{+} species are supposed, because this oxidation state has been reported before for this kind of catalyst [33].

The obtained RP values are compared in Fig. 12. Pure CeO_2 has a RP value of ca. 42%. Supports doped with Fe and Zr present higher reduction percentages, ca. 60%, whereas CeZn10, despite the possible reduction of Zn species, has a similar RP value than pure CeO_2. These data agree with the characterization results and reinforce the evidence for the formation of a solid solution in the case of CeZr10 and CeFe10 samples, leading to an increase in the ceria reducibility, and with the absence of a strong Ce–Zn interaction as a result of the ZnO segregation in the CeZn10 solid.

Upon gold, an increase in the reduction percentage is only observed for Au/CeO_2 and Au/CeFe10 catalysts. This behavior indicates a double role of gold as reducibility promoter over these solids. First, gold allows the reducing of surface Ce^{4+} species to Ce^{3+} at lower temperatures and second increases the proportion of species able to consume H_2. For the supports doped with Zr and Zn, gold only favors the reduction at lower temperatures.

The enhancement of the catalytic activity of ceria-modified gold catalysts with respect to pure CeO_2 has been already reported for the CO oxidation in WGS [39] or PROX [9,16,28]. In these studies, the catalytic activity is directly correlated with the reducibility of the solid because it favors the activation of the CO molecule over the surface. A similar explanation could be claimed in our case, since all modified solids present a higher reducibility than pure CeO_2. The CO conversion enhancement depends on the nature of the doping metal, being the more reducible support (CeFe10), the one with higher (Fig. 10). Besides this, in this solid, the contribution of the intrinsic catalytic activity of iron sites cannot be fully discarded.

The promoting effect of gold on the catalytic activity, Fig. 11, is more evident for the doped catalyst for which the CO conversion starts at temperatures below 75 °C. The similar behavior of the gold-doped catalysts (Au/CeZr10, Au/CeZn10 and Au/CeFe10) seems to indicate that the catalytic activity is independent of the type of interaction between the doping metal (Zr, Zn or Fe) and ceria that generates, annihilates or does not alter oxygen vacancies, although the catalytic activity depends on the catalyst reducibility. Similarly, Manzoli and coworkers found for Au/doped-ceria catalysts that the active sites in the PROX reaction are not the gold clusters and/or the Ce^{3+} defective sites, but the step sites of gold particles in which both CO and oxygen activation occur [64]. Therefore, for our catalysts the gold/doped-ceria interface is

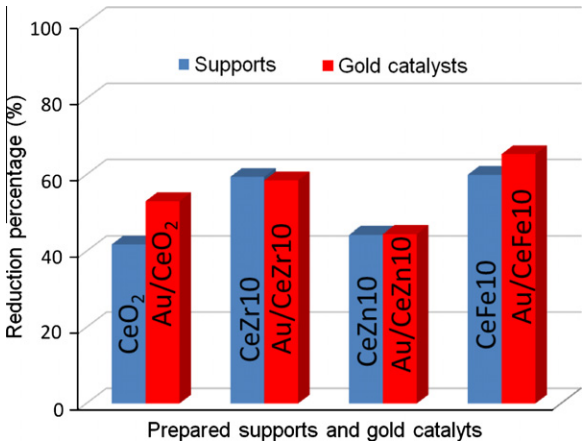

Fig. 12. Reduction percentage of the prepared solids.

responsible of the conversion of the CO molecules and consequently, oxygen vacancies are not the only mechanism to efficiently promote gold dispersion in ceria-based catalysts. In addition to this, the catalytic behavior of the gold systems confirms that the noble metal is a promoter of the oxygen exchange, especially at temperatures below 200 °C, where the PROX reaction takes place. This promotion effect on the oxygen exchange has been previously reported by Fu and coworkers [27]. These authors studying an Au/CeO_2 catalyst found a low reduction peak near 100 °C in a H_2-TPR experiment and concluded that gold facilitates the activation of surface oxygen species on the surface of the ceria surface during the water gas shift reaction [65]. Similar results were reported by Zhong and coworkers on the oxidation of CO over Au/Fe_2O_3 catalysts [66]. At the reaction temperatures below 100 °C, the reaction of CO with active surface oxygen species of the Au/Fe_2O_3 system is catalyzed by gold nanoparticles. Gold may also be responsible for the creation of these active surface oxygen species in the first instance, although it is not yet clear whether these are present on Au itself or have spilled over to the adjacent support surface.

The O_2 selectivity to the CO conversion for the gold catalysts during the PROX reaction is shown in Fig. 13. The Au/CeO_2 catalyst shows an especially high O_2 selectivity at temperatures below 160 °C in comparison with the rest of catalysts. However, in this temperature range, the CO conversion over the Au/CeO_2 catalyst is very poor (ca. 0%) compared with those of the other catalysts (Fig. 11), so a direct comparison among the selectivities is erroneous. On the other hand, above 160 °C it is observed for all catalysts that both CO conversion and O2 selectivity decrease on increasing temperature. Undesired side reactions, H_2 oxidation [67] or the reverse water gas shift [40], are favored on increasing the temperature.

The relationship between the O_2 selectivity and the CO conversion is presented in Fig. 14. Except for the values obtained for the Au/CeO_2 catalyst at temperatures lower than 160 °C (enclosed in circles), a similar linear relationship (with the same slope) between conversion and selectivity is observed for all catalysts. A similar behavior has been previously discussed by Hernández and coworkers [68] in their study of modified cryptomelane manganese dioxide for the PROX reaction. They also established the relationship between CO conversion and O_2 selectivity and proposed that for lower temperatures, where the CO conversion is far from the equilibrium conditions, there is a fast selectivity decrease as the conversion increases. At higher temperatures, where the CO conversion is close to the equilibrium conditions, a linear relationship could be established between the conversion and the selectivity. The description of both zones of this analysis is in good agreement with our results. The linear relationship observed in Fig. 14 indicates that the observed selectivity follows the thermodynamic limit.

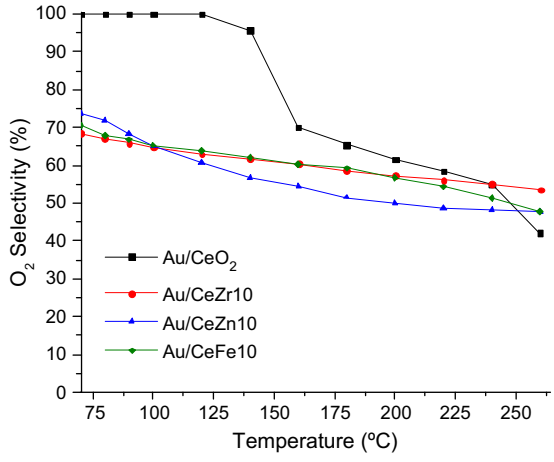

Fig. 13. O_2 selectivity to the CO conversion during the PROX reactions for the studied gold catalysts.

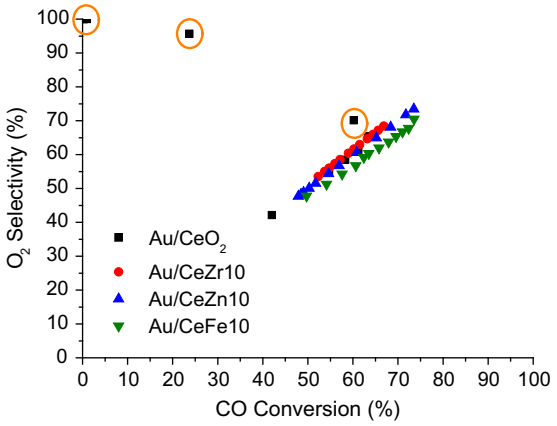

Fig. 14. Relationship between the O_2 selectivity and the CO conversion.

The best catalytic performances are obtained with the Au/CeFe10 catalyst (higher conversion at the same selectivity). From Fig. 14, it is also clear that higher the CO conversion higher the selectivity of the system, especially at low temperatures. This behavior is in good agreement with the higher activation energy of the H_2 oxidation compared with that of the CO oxidation, as was discussed by Scirè and coworkers [69], who observed a decreasing in the ratio of surface coverage of CO and H (θCO/θH) on gold particles when the temperature is increased.

Although the present study did not directly characterize the nature of the active sites of the PROX reaction, this last remark suggests that the surface coverage of these active sites by reactive molecules plays an important role in the selectivity of the process. According to this, the diffusion of molecules involved in the reaction could be crucial to encourage a more selective oxidation.

5. Conclusions

The modification of CeO_2 was successfully achieved with three doping metallic elements Zr, Zn and Fe. However, there are special features in the final materials depending on the nature of the modifier. Solid solutions are formed on doping with Zr and Fe cations, whereas ZnO segregation is observed on doping with Zn. However, an enhancement of the reducibility or the oxygen exchange ability is observed for all the doped supports. The formation of surface oxygen vacancies depends on the nature of the modifier, doping with Zr enhances the formation of surface oxygen vacancies, with Zn remains the same as for pure CeO_2 and with Fe, the oxygen vacancies disappear. Nevertheless, a high dispersion of gold nanoparticles is achieved in all cases. These results allow stating the formation of oxygen vacancies is not the only way to increase the dispersion of gold nanoparticles, as in the case of Au/CeZr10 catalyst. During the modification with Zn, the epitaxial interaction between CeO2 and ZnO could create referential sites for the deposition of gold in the interphase between the two oxides. Doping with iron results in a solid solution where the Fe ions are occupying interstitial positions in the CeO_2 structure. These low coordination positions result in electron-rich sites that replace oxygen vacancies for anchoring gold nanoparticles.

The new surface sites created upon doping result in enhanced catalytic activities for CO conversion over gold catalysts supported

on modified ceria materials. For the Au/CeM10 catalysts (M = Zr, Zn and Fe), no significant differences in CO conversion or O_2 selectivity can be pointed out. This means that CO conversion was improved by the synergy Au–Ce–M (M = Zr, Zn and Fe) regardless the nature of the modifier cation.

The obtained results allow, as a general remark, emphasize the strong relationship between the reducibility enhancement and the increase in the CO conversion. Therefore, the Au/CeFe10 catalyst showing the highest reducibility percentage among the tested catalysts results in the highest CO conversion for the synthesized catalysts.

Acknowledgments

The financial support for this work has been obtained from the Spanish Ministerio de Ciencia e Innovación (ENE2009-14522-C05-01) cofinanced by FEDER funds from the European Union and from Junta de Andalucía (P09-TEP-5454). O.H. Laguna and F. Romero-Sarria thank the same Ministry for the FPI fellowship (MAT-2006-12386-C05) and the Ramón y Cajal contract awarded, respectively. Finally, we thank Dr. Juan Almagro (ACERINOX S.A. Spain) for his help with high-resolution FESEM experiments.

References

[1] A. Demirbas, Progress in Energy and Combustion Science 31 (2005) 171–192.
[2] C. Sopena, P.M. Diéguez, D. Sáinz, J.C. Urroz, E. Guelbenzu, L.M. Gandía, International Journal of Hydrogen Energy 35 (2010) 1420–1429.
[3] G. Arzamendi, P.M. Diéguez, M. Montes, M.A. Centeno, J.A. Odriozola, L.M. Gandía, Catalysis Today 143 (2009) 25–31.
[4] R. Burch, Physical Chemistry Chemical Physics 8 (2006) 5483–5500.
[5] V. Idakiev, T. Tabakova, K. Tenchev, Z.-Y. Yuan, T.-Z. Ren, B.-L. Su, Catalysis Today 128 (2007) 223–229.
[6] T. Tabakova, V. Idakiev, J. Papavasiliou, G. Avgouropoulos, T. Ioannides, Catalysis Communications 8 (2007) 101–106.
[7] Z.-Y. Yuan, V. Idakiev, A. Vantomme, T. Tabakova, T.-Z. Ren, B.-L. Su, Catalysis Today 131 (2008) 203–210.
[8] F. Mariño, G. Baronetti, M. Laborde, N. Bion, A. Le Valant, F. Epron, D. Duprez, International Journal of Hydrogen Energy 33 (2008) 1345–1353.
[9] N. Bion, F. Epron, M. Moreno, F. Mariño, D. Duprez, Topics in Catalysis 51 (2008) 76–88.
[10] F.J. Pérez-Alonso, M. López Granados, M. Ojeda, P. Terreros, S. Rojas, T. Herranz, J.L.G. Fierro, M. Gracia, J.R. Gancedo, Chemistry of Materials 17 (2005) 2329–2339.
[11] H. Bao, X. Chen, J. Fang, Z. Jiang, W. Huang, Catalysis Letters 125 (2008) 160–167.
[12] P.J. Gellings, H.J.M. Bouwmeester, Catalysis Today 12 (1992) 1–101.
[13] G. Xiao, S. Li, H. Li, L. Chen, Microporous and Mesoporous Materials 120 (2009) 426–431.
[14] G. Avgouropoulos, T. Ioannides, Journal of Molecular Catalysis A: Chemical 296 (2008) 47–53.
[15] M. Turco, G. Bagnasco, C. Cammarano, P. Senese, U. Costantino, M. Sisani, Applied Catalysis B: Environmental 77 (2007) 46–57.
[16] G. Avgouropoulos, M. Manzoli, F. Boccuzzi, T. Tabakova, J. Papavasiliou, T. Ioannides, V. Idakiev, Journal of Catalysis 256 (2008) 237–247.
[17] T. Tabakova, V. Idakiev, D. Andreeva, I. Mitov, Applied Catalysis A: General 202 (2000) 91–97.
[18] V. Idakiev, T. Tabakova, A. Naydenov, Z.Y. Yuan, B.L. Su, Applied Catalysis B: Environmental 63 (2006) 178–186.
[19] L. Zhi Min, W. Jian Li, Z. Jun Bo, C. Yao Qiang, Y. Sheng Hui, G. Mao Chu, Journal of Hazardous Materials 149 (2007) 742–746.
[20] P. Panagiotopoulou, J. Papavasiliou, G. Avgouropoulos, T. Ioannides, D.I. Kondarides, Chemical Engineering Journal 134 (2007) 16–22.
[21] B.M. Reddy, G.K. Reddy, I. Ganesh, J.M.F. Ferreira, Journal of Materials Science 44 (2009) 2743–2751.
[22] J. Kaspar, P. Fornasiero, Structural properties and thermal stability of ceria–zirconia and related materials, in: A. Trovarelli (Ed.), Cataysis by Ceria and Related Materials, Imperial College, London, 2002, p. 217.
[23] A.S. Reddy, C.-Y. Chen, C.-C. Chen, S.-H. Chien, C.-J. Lin, K.-H. Lin, C.-L. Chen, S.-C. Chang, Journal of Molecular Catalysis A: Chemical 318 (2010) 60–67.
[24] J. Papavasiliou, G. Avgouropoulos, T. Ioannides, Applied Catalysis B: Environmental 69 (2007) 226–234.
[25] M. Haruta, N. Yamada, T. Kobayashi, S. Iijima, Journal of Catalysis 115 (1989) 301–309.
[26] A. Karpenko, R. Leppelt, V. Plzak, R.J. Behm, Journal of Catalysis 252 (2007) 231–242.
[27] Q. Fu, H. Saltsburg, M. Flytzani-Stephanopoulos, Science 301 (2003) 935–938.
[28] W.Y. Hernández, F. Romero-Sarria, M.A. Centeno, J.A. Odriozola, Journal of Physical Chemistry C 114 (2010) 10857–10865.
[29] M.I. Domínguez, F. Romero-Sarria, M.A. Centeno, J.A. Odriozola, Applied Catalysis B: Environmental 87 (2009) 245–251.
[30] F. Romero-Sarria, L.M.T. Martínez, M.A. Centeno, J.A. Odriozola, Journal of Physical Chemistry C 111 (2007) 14469–14475.
[31] H. Provendier, C. Petit, J.L. Schmitt, A. Kiennemann, C. Chaumont, Journal of Materials Science 34 (1999) 4121–4127.
[32] F. Romero-Sarria, J.C. Vargas, A.-C. Roger, A. Kiennemann, Catalysis Today 133–135 (2008) 149–153.
[33] A. Penkova, K. Chakarova, O.H. Laguna, K. Hadjiivanov, F.R. Saria, M.A. Centeno, J.A. Odriozola, Catalysis Communications 10 (2009) 1196–1202.
[34] M.Á. Centeno, C. Portales, I. Carrizosa, J.A. Odriozola, Catalysis Letters 102 (2005) 289–297.
[35] M.A. Centeno, K. Hadjiivanov, T. Venkov, H. Klimev, J.A. Odriozola, Journal of Molecular Catalysis A: Chemical 252 (2006) 142–149.
[36] E. Moretti, L. Storaro, A. Talon, P. Patrono, F. Pinzari, T. Montanari, G. Ramis, M. Lenarda, Applied Catalysis A: General 344 (2008) 165–174.
[37] W.Y. Hernández, M.A. Centeno, F. Romero-Sarria, J.A. Odriozola, Journal of Physical Chemistry C 113 (2009) 5629–5635.
[38] Z.Y. Pu, J.Q. Lu, M.F. Luo, Y.L. Xie, Journal of Physical Chemistry C 111 (2007) 18695–18702.
[39] A. Fonseca, J. Fisher, D. Ozkaya, M. Shannon, D. Thompsett, Topics in Catalysis 44 (2007) 223–235.
[40] G.W. Roberts, P. Chin, X. Sun, J.J. Spivey, Applied Catalysis B: Environmental 46 (2003) 601–611.
[41] C. Mondelli, V.D. Santo, A. Trovarelli, M. Boaro, A. Fusi, R. Psaro, S. Recchia, Catalysis Today 113 (2006) 81–86.
[42] S. Rossignol, C. Micheaud-Especel, D. Duprez, F.V.M.S.M. Avelino Corma, G.F. José Luis, Structural and catalytic properties of Zr–Ce–O mixed oxides. Role of the anionic vacancies, in: Studies in Surface Science and Catalysis, Elsevier, 2000, pp. 3327–3332.
[43] F.J. Perez-Alonso, I. Melián-Cabrera, M. López Granados, F. Kapteijn, J.L.G. Fierro, Journal of Catalysis 239 (2006) 340–346.
[44] J.E. Spanier, R.D. Robinson, F. Zhang, S.W. Chan, I.P. Herman, Physical Review B – Condensed Matter and Materials Physics 64 (2001) 2454071–2454078.
[45] Q. Fu, W. Deng, H. Saltsburg, M. Flytzani-Stephanopoulos, Applied Catalysis B: Environmental 56 (2005) 57–68.
[46] Z.-Y. Pu, J.-Q. Lu, M.-F. Luo, Y.-L. Xie, The Journal of Physical Chemistry C 111 (2007) 18695–18702.
[47] P. Singh, M.S. Hegde, Journal of Solid State Chemistry 181 (2008) 3248–3256.
[48] T. Masui, Y. Peng, K.-i. Machida, G.-y. Adachi, Chemistry of Materials 10 (1998) 4005–4009.
[49] A. Trovarelli, Comments on Inorganic Chemistry 20 (1999) 263–284.
[50] S. Damyanova, B. Pawelec, K. Arishtirova, M.V.M. Huerta, J.L.G. Fierro, Applied Catalysis A: General 337 (2008) 86–96.
[51] E.V. Ramos-Fernández, A.F.P. Ferreira, A. Sepúlveda-Escribano, F. Kapteijn, F. Rodríguez-Reinoso, Journal of Catalysis 258 (2008) 52–60.
[52] M. Consonni, D. Jokic, D. Yu, D. Yu Murzin, R. Touroude, Journal of Catalysis 188 (1999) 165–175.
[53] P. Naknam, A. Luengnaruemitchai, S. Wongkasemjit, Energy & Fuels 23 (2009) 5084–5091.
[54] S. Li, S. Krishnamoorthy, A. Li, G.D. Meitzner, E. Iglesia, Journal of Catalysis 206 (2002) 202–217.
[55] M.I. Domínguez, M. Sánchez, M.A. Centeno, M. Montes, J.A. Odriozola, Journal of Molecular Catalysis A: Chemical 277 (2007) 145–154.
[56] Z. Kónya, V.F. Puntes, I. Kiricsi, J. Zhu, J.W. Ager, M.K. Ko, H. Frei, P. Alivisatos, G.A. Somorjai, Chemistry of Materials 15 (2003) 1242–1248.
[57] M.A. Centeno, M.C. Hidalgo, M.I. Domínguez, J.A. Navío, J.A. Odriozola, Catalysis Letters 123 (2008) 198–206.
[58] K. Qian, S. Lv, X. Xiao, H. Sun, J. Lu, M. Luo, W. Huang, Journal of Molecular Catalysis A: Chemical 306 (2009) 40–47.
[59] A. Khan, P.G. Smirniotis, Journal of Molecular Catalysis A: Chemical 280 (2008) 43–51.
[60] G. Jacobs, S. Ricote, P.M. Patterson, U.M. Graham, A. Dozier, S. Khalid, E. Rhodus, B.H. Davis, Applied Catalysis A: General 292 (2005) 229–243.
[61] C.H. Kim, L.T. Thompson, Journal of Catalysis 230 (2005) 66–74.
[62] W. Deng, A.I. Frenkel, R. Si, M. Flytzani-Stephanop, Journal of Physical Chemistry C 112 (2008) 12834–12840.
[63] T. Tabakova, F. Boccuzzi, M. Manzoli, J.W. Sobczak, V. Idakiev, D. Andreeva, Applied Catalysis A: General 298 (2006) 127–143.
[64] M. Manzoli, G. Avgouropoulos, T. Tabakova, J. Papavasiliou, T. Ioannides, F. Boccuzzi, Catalysis Today 138 (2008) 239–243.
[65] Q. Fu, S. Kudriavtseva, H. Saltsburg, M. Flytzani-Stephanopoulos, Chemical Engineering Journal 93 (2003) 41–53.
[66] Z. Zhong, J. Highfield, M. Lin, J. Teo, Y.-f. Han, Langmuir 24 (2008) 8576–8582.
[67] B. Schönbrod, F. Mariño, G. Baronetti, M. Laborde, International Journal of Hydrogen Energy 34 (2009) 4021–4028.
[68] W.Y. Hernández, M.A. Centeno, F. Romero-Sarria, S. Ivanova, M. Montes, J.A. Odriozola, Catalysis Today (2010), doi:10.1016/j.cattod.2010.03.010.
[69] S. Scirè, C. Crisafulli, S. Minicò, G.G. Condorelli, A. Di Mauro, Journal of Molecular Catalysis A: Chemical 284 (2008) 24–32.